

# The Role of Sample Geometry on Ultra-Low Alpha Particle Emissivity Measurements

Michael S. Gordon, *Senior Member, IEEE*, Kenneth P. Rodbell, *Senior Member, IEEE*,  
Conal E. Murray, and Brendan D. McNally, *Member, IEEE*

**Abstract**—The detection efficiency of an ionization counter and the resulting energy spectra of samples can be dependent on the sample geometry. This is especially important for samples that are large compared to the size of the detector since some of the alpha particles emitted near the edge of the samples might not be collected if their trajectories fall outside the active area of the detector. We examine this effect in detail by measuring the alpha particles detected for rings and disks of various sizes, and compare the results to analytical and Monte Carlo models.

**Index Terms**—Alpha particles, ionization detector, ultra-low background.

## I. INTRODUCTION

IN ORDER to have acceptable single event upset rates (SER), materials in use for fabricating semiconductors must have alpha particle emission rates in the ultra-low emission (ULA) range of  $< 2\alpha/\text{KHR}\cdot\text{cm}^2$  [1]. Making measurements of these materials in a timely manner requires large area samples, low detector backgrounds, and alpha particle counters with high detection efficiency [2]. In this paper, we discuss the topic of detection efficiency for samples in a commercially-available ionization detector.

The detection efficiency of alpha particles in ionization detectors can approach unity provided that the alpha particles stop within the detector's active counting region. In the XIA UltraLo-1800 counter, the active counting region is defined by the geometry of the anode electrode, while the guard electrode, located coaxially with the anode at the top of the counter, defines the veto region [3]–[6]. Efficiency is lost (e.g. alpha particles are rejected) when the tracks created from the ionization of the counter gas fall outside of the active counting region, which can occur when the alpha particles are emitted from the outer portions of large samples.

For an *isotropic*, alpha particle-emitting point source, the detection efficiency will approach 1/2 as the source is moved toward the boundary between the active and veto regions of the detector [3], [6]. This is because at the boundary half of the alpha particle emissions will have trajectories that are contained within the active region while half fall outside into the veto region. So all of the alpha particles from small samples will be detected with unity efficiency;

however some alpha particles will not be counted from large samples, depending on their trajectory.

For this reason, the software in the XIA UltraLo-1800 ionization detector reports an *energy-dependent* efficiency for each alpha particle detected, assuming *isotropic* emission, and further assuming the sample size is either 707 cm<sup>2</sup> (300 mm diameter) or an 1800 cm<sup>2</sup> square (42.4 cm × 42.4 cm), corresponding to the two operating modes of the detector. The alpha particle emissivity ( $\alpha/\text{KHR}\cdot\text{cm}^2$ ) is computed for these samples sizes given the energy-dependent efficiency for each of the alpha particles counted [3].

This paper will discuss the interesting region between small and large sample sizes, and the effect that the alpha particle energies have on their detection. First, representative data from small and large samples will be presented. Then a discussion of the trends in the data is given. Next, a summary of modeling of the energy-dependent efficiency is presented, and finally a summary and conclusion is presented with guidance for measuring large or uniquely shaped samples.

## II. EXPERIMENTAL DETAILS

In the experiments described in this work, we used the *natural* alpha-particle radiation from aluminum and lead samples, rather than using radioactive sources, to examine the counting rate, alpha particle emissivity and the energy spectra as a function of sample size. The materials used for these samples were “off-the-shelf,” commercially-available materials. The XIA UltraLo-1800 ionization counter was operated in the “wafer” mode (300 mm diameter, 707 cm<sup>2</sup>) to demonstrate the effect of sample size, and in the “full” mode (1800 cm<sup>2</sup>) to obtain the absolute emissivity for the large samples. A schematic of the counter is shown in Fig. 1 and the operation the operation is described in [3].

In the first set of experiments, we machined three aluminum rings of the same area, *from the same piece of initial stock*. This is important due to questions that arise about the uniformity of the material if the samples had been machined from different initial pieces of stock. All things being equal, we would expect the emission rate (and emissivity) to be identical for these samples. The dimensions of the rings were (outer diameter-inner diameter): 300 mm-280 mm, 260 mm-236.7 mm and 200 mm-168.5 mm respectively. The rings had an area of 91.1 cm<sup>2</sup>. The thickness of these aluminum samples was 0.032”.

The second set of experiments examined the emission from aluminum rings of varying diameters where the web (outer radius– inner radius) was kept at a constant 0.5 cm. These rings were machined from a single 300 mm outer

Manuscript received July 8, 2016; revised October 10, 2016; accepted October 25, 2016. Date of publication December 2, 2016; date of current version February 28, 2017.

M. S. Gordon, K. P. Rodbell, and C. E. Murray are with IBM T.J. Watson Research Center, Yorktown Heights, NY 10598 USA (e-mail: gordonm@us.ibm.com).

B. D. McNally is with XIA LLC, Hayward, CA 94544 USA.

Color versions of one or more of the figures in this paper are available online at <http://ieeexplore.ieee.org>.

Digital Object Identifier 10.1109/TNS.2016.2634542

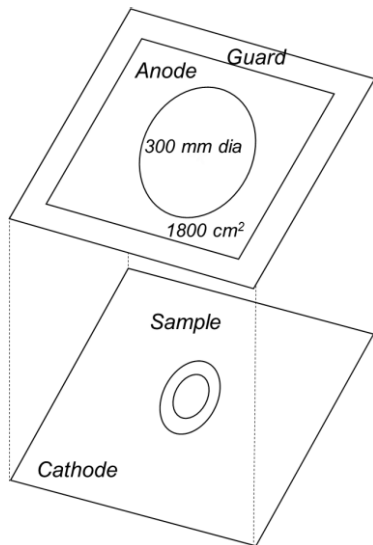


Fig. 1. Schematic of the UltraLo-1800.

diameter piece. The expectation for these samples was that although the emission rate would be different (since the rings had different areas), the emissivity would be constant. The outer diameter of these rings were: 300mm, 275mm, 250mm, 225mm, 200mm, and 175mm. The thickness of the aluminum samples was also 0.032”.

The third set of experiments investigated the alpha particle emission from continuous aluminum disks with 300 mm and 200 mm diameters, from the same piece of initial stock. Once again, the thickness of the aluminum samples was 0.032”.

The final experiment considered the alpha particle emission from lead disks with 300 mm and 200 mm diameters, and a ring with 200 mm inner diameter and 300 mm outer diameter. The 200 mm diameter disk, and the ring was made from the one 300 mm diameter piece of material. The thickness of the lead samples was 0.0025”.

### III. EXPERIMENTAL RESULTS

For all of the experiments with the aluminum rings, and the aluminum disks, the samples were placed on either a 300 mm diameter silicon wafer or a tray liner whose emissivity was  $\sim 0.5$   $\alpha/\text{hr}\cdot\text{cm}^2$ . For completeness, the emission rate from either the wafer or the tray liner was subtracted and the errors due to counting statistics were propagated. The lead disks and ring were placed on either a 300 mm or 200 mm wafer. Since the emission rate from the lead was several orders of magnitude larger than the silicon wafer, the background from the silicon wafer was not subtracted.

The alpha particle emissivity and emission rate data for the rings of equal area are shown in Fig. 2. The data shown in black are the emissivity data (left-hand scale), and the corresponding emission rate data are shown in red (right-hand scale). The solid data points connected by solid lines correspond to the samples being measured in the “wafer” mode (eg.  $707\text{cm}^2$ ). The open data points connected by the dashed lines correspond to the samples being measured in the “full” mode (eg.  $1800\text{cm}^2$ ).

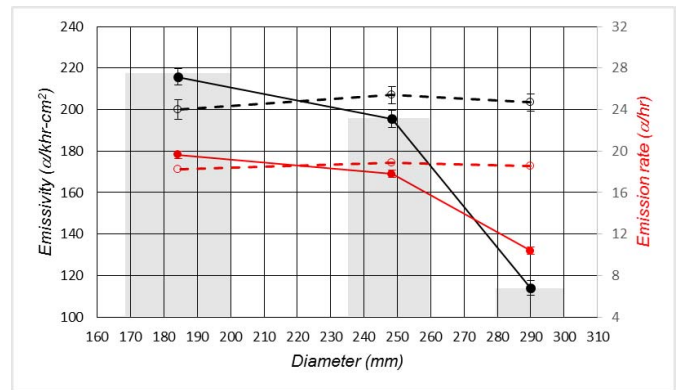


Fig. 2. The emissivity and emission rate data for the equal size Al rings. Solid data points connected by solid lines correspond to “wafer” mode, and open data points connected by dashed lines correspond to “full” mode.

The shaded areas show the range in size of the rings from the inner to the outer diameter and the data are plotted at the value of the mean diameter. Because the sample geometry did not conform to the manufacturer’s assumptions, the emissivity was computed from the raw data only, *assuming the detection efficiency was unity* and simply represents a rescaling of the count rate from  $\alpha/\text{hr} \rightarrow \alpha/\text{kr}\cdot\text{cm}^2$ . The error bars represent  $\pm 1\sigma$  from the counting statistics.

For the data taken in “wafer” mode (solid data points, solid lines), the emissivity was *largest* for the *smallest* ring and was about twice the value of the largest ring where the emissivity was about  $220$   $\alpha/\text{kr}\cdot\text{cm}^2$  which is  $\sim 100\text{X}$  the ULA specification. Nominally, in a larger detector, one would expect that the counting rate, and emissivity, would be identical for each of the rings since they possess the same area and were made from the same initial piece of stock. The data from when these samples were measured in “full” mode (open data points, dashed lines), confirm a constant alpha particle emission rate, and emissivity. As expected, the observed decrease in “raw” emissivity and counting rate with the larger samples is due to reduced detection efficiency for these large samples, when measured in “wafer” mode.

Figs. 3a shows histograms of the alpha particle energy distribution for the smallest ring (top), the middle ring (middle) and the largest ring (bottom) when measured in “wafer” mode. These histograms have not been corrected for efficiency losses. The alpha particle data were partitioned into 0.2 MeV wide bins, and the data shown in the figure are in units of counts/ hr/ 0.2 MeV bin. Of course, the total alpha particle count rate from the sample is the integral of the data in the spectra. The main difference in the histograms in Figs. 3a is the pronounced peak for the smallest ring consistent with emission from  $^{210}\text{Po}$ , (normally seen in Pb or Sn-based samples [7]–[9]), the attenuated peak for the middle ring, and the lack of a peak for the largest ring. One question to be answered by this work is- “why does the structure of the observed energy spectra appear to change with sample geometry?”

Shown in Figs. 3b are the same energy spectra (histograms) for the same rings, when measured in the “full” mode. Peaks from  $^{210}\text{Po}$  appear in each of the spectra. The peaks are broader than those from Figs. 3a, due to more noise on the

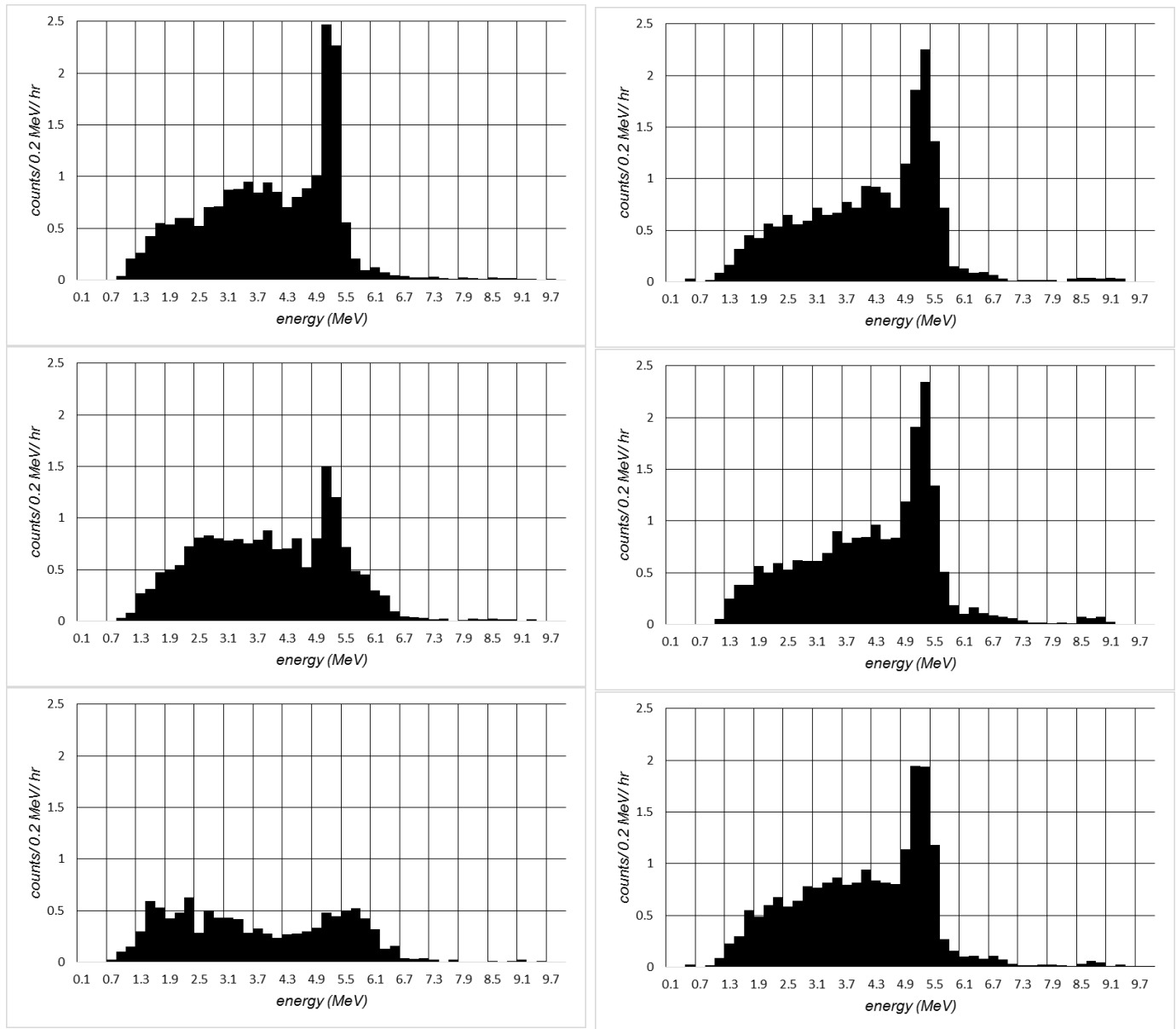


Fig. 3. (a) (left column) Alpha particle energy spectra from the smallest ring (top), middle ring (middle) and the largest ring (bottom). The rings have equal area and were measured in “wafer” mode. (b) (right column) Alpha particle energy spectra from the smallest ring (top), middle ring (middle) and the largest ring (bottom). The rings have equal area and were measured in “full” mode.

signals, which is caused by the increased capacitance of the counter’s anode in “full” mode. Clearly, the fact that the peak went away for the largest sample, when measured in “wafer” mode, indicates that the detector has rejected these alpha particles emitted at large angles.

A complete discussion of the origin and diffusion of  $^{210}\text{Po}$  in samples is beyond the scope of this paper. However, a recent review article on contaminants in semiconductor materials discusses these topics in detail [10].

The alpha particle emissivity and emission rate data for the second experiment (aluminum rings with outer diameter minus inner diameter of 1 cm) are shown in Fig. 4. As with Fig. 2, the solid data points connected with solid lines are data taken in the “wafer” mode, and the open data points connected with dashed lines are data taken for the same rings

in the “full mode. The black data points are the emissivity data (left-hand scale), and the emission rate data are given in red (right-hand scale). The data are plotted at the mean diameter of each ring and the error bars represent  $\pm 1\sigma$  from the counting statistics. For reasons similar to the first experiment, the emissivity was computed without an efficiency correction (assuming the efficiency was unity for each alpha particle detected).

For the data taken in “wafer” mode (solid points connected with solid lines), the emissivity was essentially constant at  $\sim 200 \pm 10 \text{ } \alpha/\text{hr}\cdot\text{cm}^2$  for the smallest four rings (outer diameter: 175 mm, 200 mm, 225 mm and 250 mm), then dropped markedly for the two larger rings where the emissivity for the largest ring was  $\sim \frac{1}{2}$  that of the smallest four rings. The data taken in “full” mode (open data points connected by

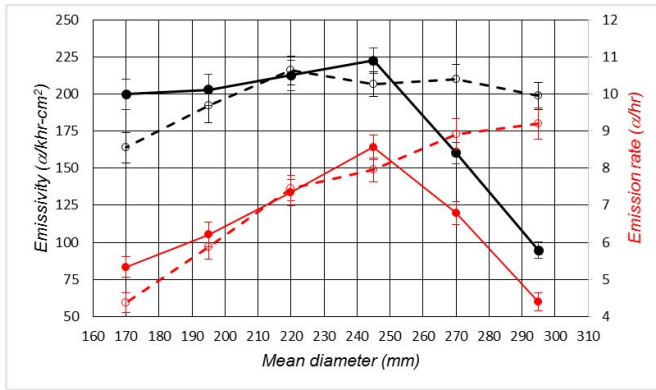


Fig. 4. The emissivity and emission rate data for the Al rings with fixed outer diameter minus inner diameter of 1 cm. Solid data points connected by solid lines correspond to “wafer” mode, and open data points connected by dashed lines correspond to “full” mode.

dashed lines) show a nearly constant alpha particle emissivity. The data point for the “full” mode at a mean diameter of 170 cm is lower than the other. This might be due to the low count rate compared to the background.

Figs. 5 shows histograms of the alpha particle energy, but with frequency scaled to *emissivity*, rather than the count rate as in Figs. 3, (since these rings have unequal area) for the 200 mm outer diameter (top) and 300 mm outer diameter (bottom) rings. In Figs. 5a we show data from the “wafer” mode, and in Figs. 5b, we show data taken in the “full” mode. As with Fig. 3, the energy bin widths are 0.2 MeV, however, the units on the vertical axes of the spectra in Figs. 5 are  $\alpha/\text{KHR}\cdot\text{cm}^2/0.2\text{ MeV}$ . Integrating the data in the spectra yields the sample’s total emissivity.

These data are qualitatively similar to these shown in Figs. 3, namely in the “wafer” mode, (Figs. 5a) the histogram of the 200 mm outer diameter (top) ring shows evidence of  $^{210}\text{Po}$ , whereas that of the 300 mm outer diameter (bottom) ring does not. Although the  $^{210}\text{Po}$  peak is not prominent in the 300 mm outer diameter ring when measured in the “full” mode, clearly there is evidence of the Po that is not present when this ring was measured in the “wafer” mode.

In order to examine whether the small vs large rings exaggerate the effect of the change in the energy spectra shown earlier (Figs. 3 and 5, top vs bottom), particularly in the “wafer” mode, the next pair of experiments used large-area disks instead of small-area rings.

The alpha particle emissivity from the 200 mm and 300 mm diameter aluminum disks for both measurement modes is given below in Table 1. Of note is that the alpha particle emissivity for these cases are all very similar. We will discuss how these data differ, compared to the rings data shown earlier, in section IV, where we discuss the efficiency models. Additionally, none of the energy spectra for any of the 4 cases shown in Table 1 shows any evidence of  $^{210}\text{Po}$  (eg no peaks at 5.3 MeV).

Histograms of the alpha particle energy of the lead disks are shown in Figs. 6 for the 200 mm diameter disk (top), and the 300 mm diameter disk (bottom). Figs. 6a shows the data taken in “wafer” mode, and Figs. 6b shows the data taken in

TABLE I  
ALPHA PARTICLE EMISSIVITY DATA FOR 200 mm DIAMETER  
AND 300 mm DIAMETER ALUMINUM DISKS<sup>1</sup>

| Al disk diameter | Measurement Mode | Emissivity ( $\alpha/\text{KHR}\cdot\text{cm}^2$ ) |
|------------------|------------------|--|
| 200 mm           | Full             | 253 +/- 5  |
|                  | Wafer            | 283 +/- 4  |
| 300 mm           | Full             | 264 +/- 3  |
|                  | Wafer            | 245 +/- 3  |

TABLE II  
ALPHA PARTICLE EMISSIVITY DATA FOR 200 mm DIAMETER  
AND 300 mm DIAMETER LEAD DISKS<sup>1</sup>

| Pb disk diameter | Measurement Mode | Emissivity ( $\alpha/\text{KHR}\cdot\text{cm}^2$ ) |
|------------------|------------------|--|
| 200 mm           | Full             | 588 +/- 8  |
|                  | Wafer            | 623 +/- 5  |
| 300 mm           | Full             | 570 +/- 8  |
|                  | Wafer            | 540 +/- 4  |

“full” mode. The signature of  $^{210}\text{Po}$  is evident in these histograms from both disks, in both measurement modes. We had expected to observe the peaks in the Pb samples, since  $^{210}\text{Pb}$ , present in Pb samples, decays to  $^{210}\text{Po}$  (through two  $\beta$ -decays), but the magnitude of the peak, relative to the emissivity at lower energy, is significantly larger for the 200 mm disk compared to the larger disk, when measured in “wafer” mode (e.g. Figs. 6a top vs bottom).

By comparing Figs. 6a, to either Figs. 5a or Figs. 3a, we see that the energy spectra for disks (containing  $^{210}\text{Po}$ ) show evidence of a peak when the samples have 300 mm OD and are measured in wafer mode, unlike the rings. The peak is present for the disks since there are significant numbers of alpha particles that are detected with high efficiency from emissions farther from the boundary.

The alpha particle emissivity from the 200 mm and 300 mm diameter Pb disks for both measurement modes is given below in Table 2. Again, the alpha particle emissivity for these cases are all very similar. We will discuss how these data differ, compared to the rings data shown earlier, in section IV, where we discuss the efficiency models.

#### IV. EFFICIENCY MODELS

The alpha particle *range* is governed by the argon gas pressure (1 atm) in the detector and the alpha particle energy. Fig. 7 shows the results from an SRIM simulation which gives the range of alpha particles vs energy in argon [11]. For reference, 5.3 MeV (from  $^{210}\text{Po}$ ) alpha particles have a range of about 4 cm in argon while the range increases to about 10.5 cm for 10 MeV alpha particles.

An *analytical* model was developed to determine the detection efficiency when the counter is operated in “wafer” mode, in which the anode diameter is 300mm. The model treats

<sup>1</sup>The low energy threshold was raised to 2.5 MeV for these measurements.

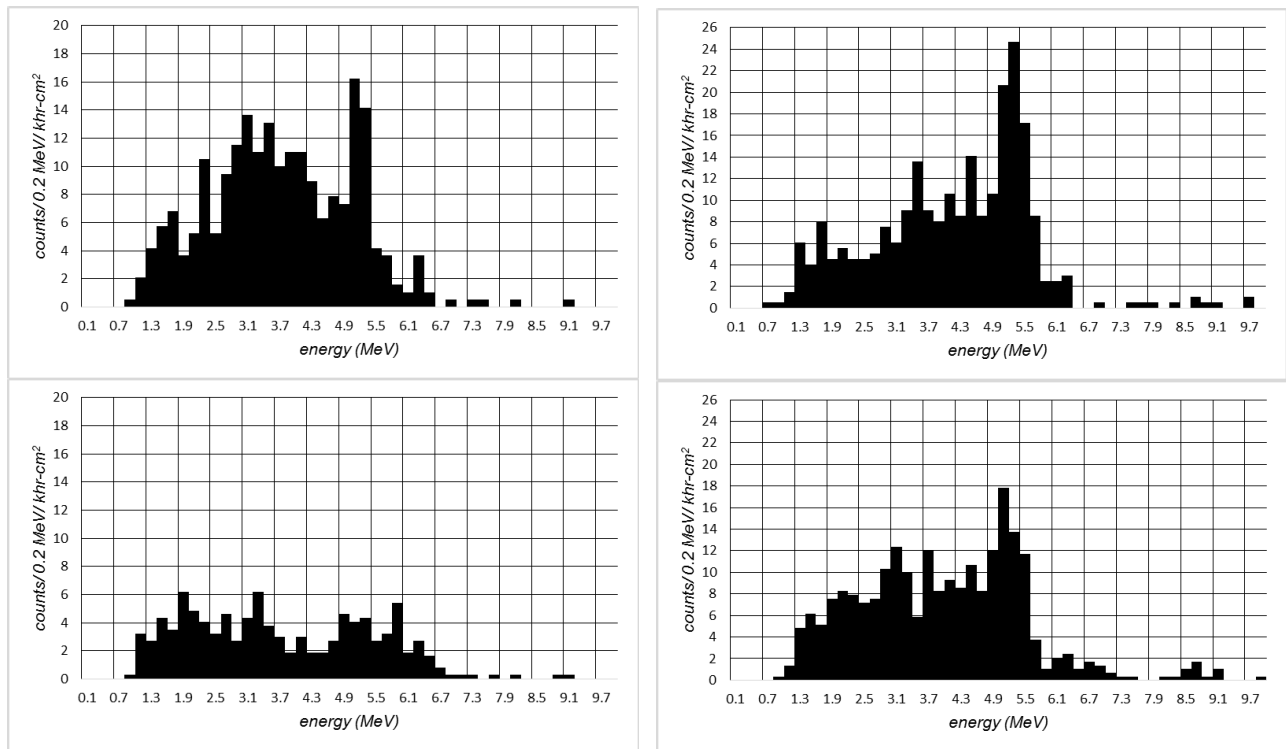


Fig. 5. (a) (left column) Alpha particle emissivity spectra from the 200 mm outer dia. (top) and the 300 mm outer dia. (bottom) rings. The rings were measured in “wafer” mode. (b) (right column) Alpha particle emissivity spectra from the 200 mm outer dia. (top) and the 300 mm outer dia. (bottom) rings. The rings were measured in “full” mode.

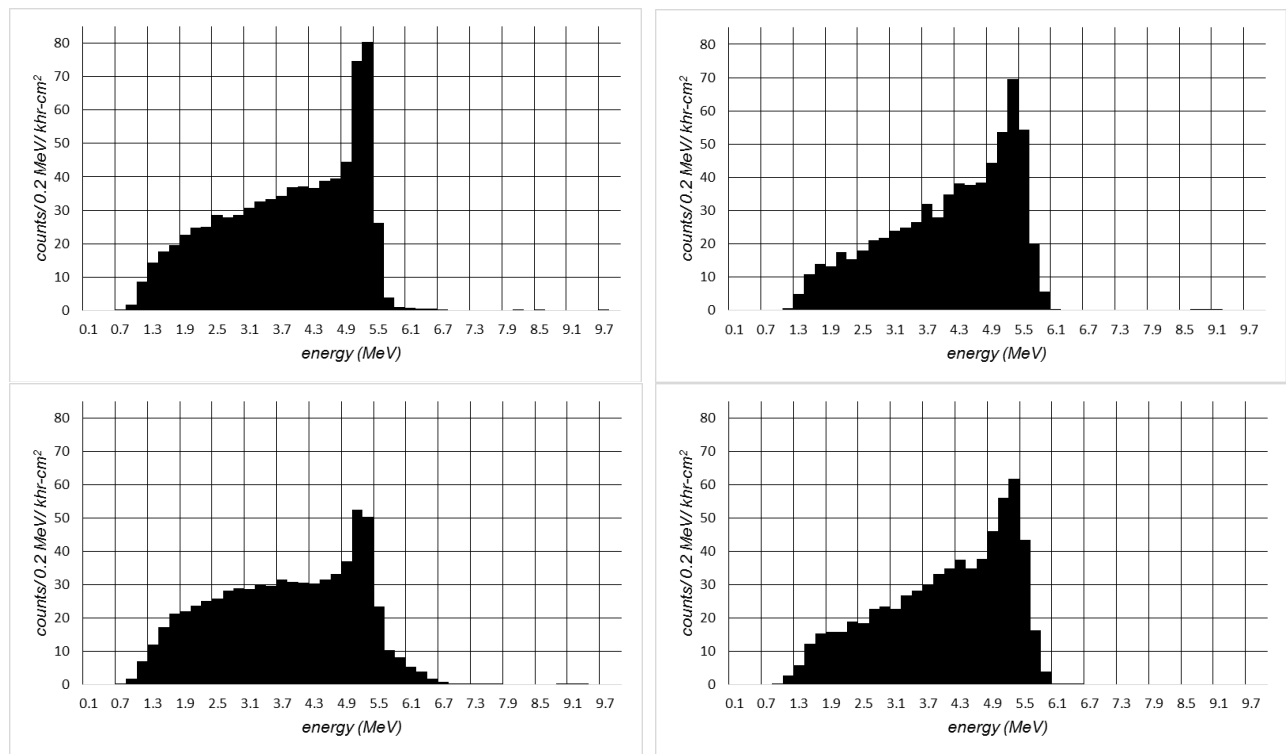


Fig. 6. (a) (left column) Alpha particle emissivity spectra from the 200 mm dia. lead disk (top) and the 300 mm dia. lead disk (bottom). The disks were measured in “wafer” mode. (b) (right column) Alpha particle emissivity spectra from the 200 mm dia. lead disk (top) and the 300 mm dia. lead disk (bottom). The disks were measured in “full” mode.

all possible paths of an emitted alpha particle with a given range,  $l$ , which is dictated by its energy, as a hemisphere. This approach is in contrast with those that calculate the

solid angle subtended by the entrance of a detector that is coaxial [12]–[14] with or arbitrary aligned [15] to a parallel, circular source. The essential difference involves the finite

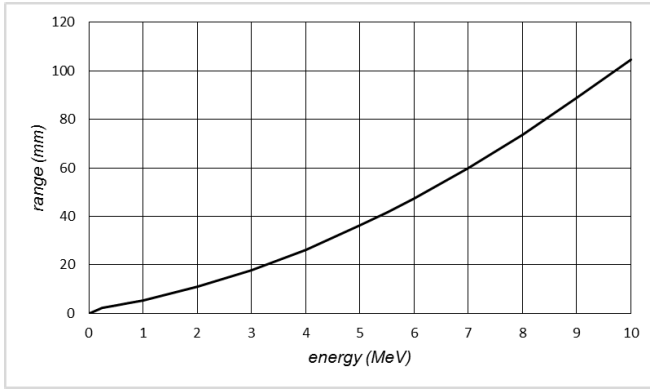


Fig. 7. The alpha particle range in argon at 1 atm. vs energy.

path length,  $l$ , of the particles which are travelling within the detector. If we assume that the detector anode can be represented by a solid circle of radius,  $r$ , the efficiency of a single particle emanating from a radial position,  $x < r$ , is equal to the relative fraction of the surface area of the hemisphere that resides within  $r$ . When  $(r-x) > l$ , the entire hemisphere is contained within  $r$  and the detection efficiency is 1. For all other cases, the hemisphere can be divided into 3 sections (as shown in Fig. 8a): a cap and lower portion corresponding to the particle trajectories that are captured by the anode, and a secondary lower portion in which the particle travels outside of the anode. By using trigonometry, we determine the relative fraction of the cap to be equal to  $1 - \sin(\theta_0)$ , where  $\theta_0 = \cos^{-1}(\frac{r-x}{l})$  represents the azimuthal angle corresponding to the bottom of the hemispherical cap. For the lower portion, we first construct a triangle as shown in Fig. 8b to determine the point at which the anode radius,  $r$ , intersects the hemisphere as a function of height from the sample surface,  $l \cos(\theta)$ . The relative fraction of the lower portion can be calculated by the following surface integral:

$$\begin{aligned} & \frac{1}{2\pi} \int_0^{\theta_0} \int_{\alpha(\theta)}^{2\pi-\alpha(\theta)} \cos(\theta) d\theta d\phi \\ &= \frac{1}{\pi} \int_0^{\theta_0} [\pi - \alpha(\theta)] \cos(\theta) d\theta \end{aligned}$$

where  $\alpha(\theta)$  is the in-plane angle corresponding to the intersection between  $r$  and the projection of the particle track with azimuthal angle,  $\theta$ . The law of cosines can be used to generate an expression for  $\alpha(\theta)$ :

$$\cos(\alpha) = \frac{r^2 - x^2 - l^2 \cos^2(\theta)}{2xl \cos(\theta)} \quad (1)$$

Combining the contributions from the cap and the lower portion, we arrive at the following expression for the efficiency,  $\Phi$ , of a particle with range  $l$  and radial position  $x$ :

$$\Phi(x, l) = \begin{cases} 1 & x \leq r - l \\ 1 - \frac{1}{\pi} \int_0^{\theta_0} \alpha(\theta) \cos(\theta) d\theta & x > r - l \end{cases}$$

The total efficiency is calculated by integrating  $\Phi(x, l)$  over the sample area. For example, a disk of radius,  $d_0$ , possesses

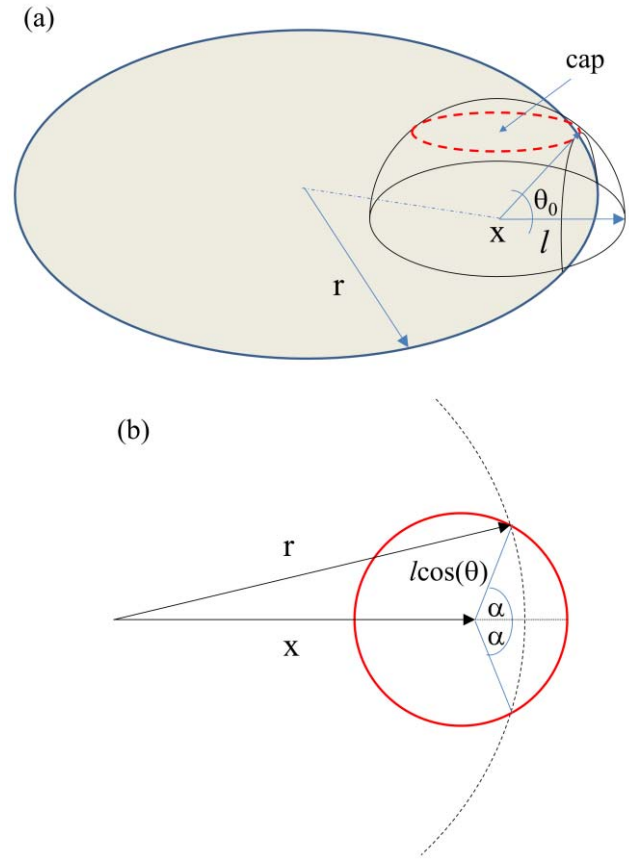


Fig. 8. (a) Schematic of a particle emitted from radial position,  $x$ , on a sample surface. The detector anode is represented by a circle of radius,  $r$ . The hemisphere of radius  $l$  corresponds to the range of the particle as dictated by its energy. The detector efficiency can be calculated by considering the relative fraction of the surface area of the hemisphere that is contained within  $r$ . (b) Top-down schematic of the method used to calculate the in-plane angle,  $\alpha(\theta)$  and thereby the lower portion of the hemisphere that contributes to the detector efficiency.

the following total efficiency:

$$\frac{2\pi \int_0^{d_0} x \Phi(x, l) dx}{\pi d_0^2}$$

and a ring of inner and outer radius,  $d_i$  and  $d_o$ , respectively, is:

$$\frac{2\pi \int_{d_i}^{d_o} x \Phi(x, l) dx}{\pi (d_o^2 - d_i^2)}$$

In order to better interpret our data, we have used the analytical model to predict the detector efficiency for the rings and disks, whose alpha particle emissivity data were measured. The results of the model are energy-dependent efficiencies- which are unique for the specific geometries. In Fig. 9, we show the results of the model for a 300 mm OD disk (case a, black line), a 200 mm OD disk (case b, red line), and a 200 mm ID, 300 mm OD ring (case c, blue line). Results from a Monte Carlo model (discussed later) for the 300 mm OD disk are shown as black dots at the center of the energy bins (shaded regions).

For case a (300 mm OD disk), the efficiency falls off monotonically for  $E > 0$  MeV as expected since the outer

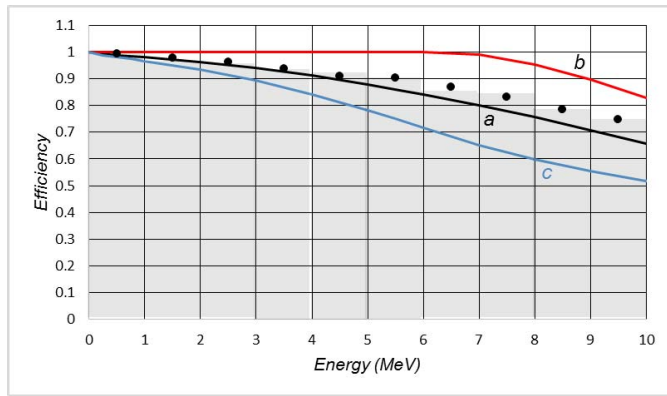


Fig. 9. The calculated efficiency vs alpha particle energy for disks of various sizes: (a) 300 mm OD, (b) 200 mm OD, and (c) 200 mm ID, 300 mm OD.

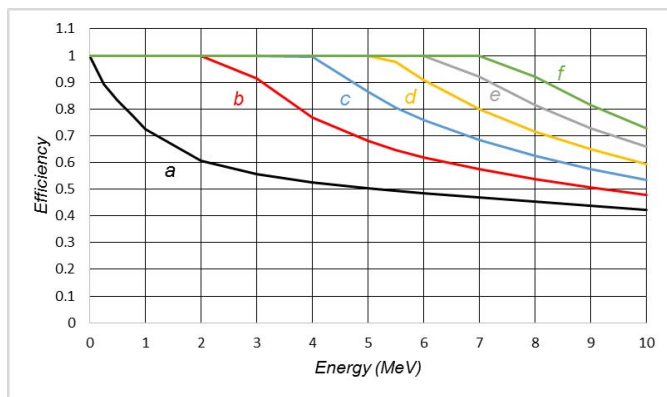


Fig. 10. The calculated efficiency vs alpha particle energy for rings with OD-ID of 1 cm: (a) 300 mm OD, (b) 275 mm OD, (c) 250 mm OD, (d) 225 mm OD, (e) 200 mm OD and (f) 175 mm OD.

diameter is at the edge of the counter's active detection region. For case b (200 mm OD disk), the efficiency is unity until  $\sim E > 7$  MeV then falls off slightly. This makes sense since alpha particles with energy  $< 6$  MeV, even if they are emitted at the edge of the disk, do not have the range to reach the boundary of the counter's active detection region, see Fig. 7. Lastly, in case c (200 mm ID, 300 mm OD ring) the efficiency falls off faster with energy, compared to case a (300 mm OD) which is easily understood since the *average* location of emissions from this ring is much closer to the boundary than the 300 mm OD disk.

In Fig. 10, we show the results of the analytical model for the six rings with OD-ID of 1 cm; 300 mm OD disk (case a, black line), 275 mm OD (case b, red line), 250 mm OD (case c, blue line), 225 mm OD (case d, orange line), 200 mm OD (case e, grey line) and 175 mm OD, (case g, green line). One observes the following trends: (1) as the outer diameter becomes larger (case f to case a), the energy threshold at which the efficiency becomes less than 1 drops to lower energy, (2) for the model results based on the 300 mm OD ring (case a), the efficiency drops dramatically from unity, even for very low alpha particle energies, (3) for high energy alpha particles,  $E > 5$  MeV, the efficiency drops below 0.5 for the 300 mm OD ring (case a), as expected since it is a narrow ring, with the outer diameter at the edge of the detector.

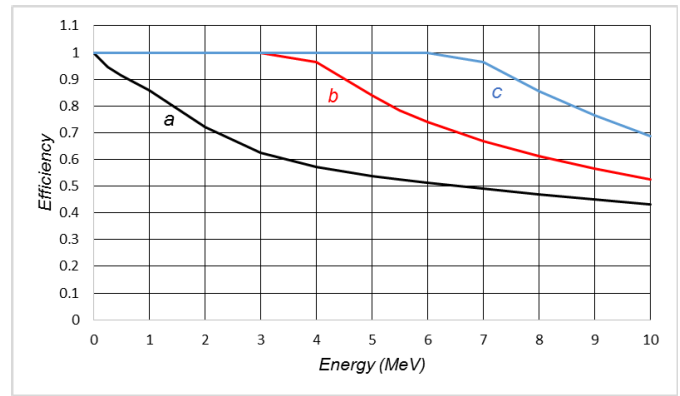


Fig. 11. The calculated efficiency vs alpha particle energy for rings with equal area ( $91.1 \text{ cm}^2$ ): (a) 300 mm OD, 280 mm ID, (b) 260 mm OD, 236.7 mm ID, (c) 200 mm OD, 168.5 mm ID.

Lastly, in Fig. 11, we show the analytical model results for the rings of equal area ( $91.1 \text{ cm}^2$ ): 300 mm OD, 280 mm ID disk (case a, black line), a 260 mm OD, 236.7 mm ID disk (case b, red line), and a 200 mm OD, 168.5 mm ID ring (case c, blue line).

Comparing case a in Fig. 10 (300 mm OD, 290 mm ID), case a in Fig. 11 (300 mm OD, 280 mm ID) and case a in Fig. 9 (300 mm diameter disk), and one sees that the effect of decreasing the inner diameter is to decrease the abrupt drop of efficiency with alpha particle energy. Similarly, comparing case e in Fig. 10 (200 mm OD, 190 mm ID), case c in Fig. 11 (200 mm OD, 168.5 mm ID), and case b in Fig. 9 (200 mm diameter disk), one immediately sees that the effect of decreasing the inner diameter of the ring increases the energy at which the efficiency drops below unity. This is to be expected since as the inner diameter is reduced, more alpha particles will stop within the active region of the detector.

We have also developed a Monte-Carlo model of the detector's efficiency and applied it to several of the samples whose alpha particle emission rate (emissivity) was measured. First, the alpha particle range vs particle energy (see Fig. 7) was parameterized by fitting the SRIM calculation with a third-order polynomial:  $R(\text{mm}) = 0.66E^2 + 3.78E + 0.8$ ; ( $R^2 = 0.9999$ ). The emission location of the alpha particles in the model was randomly chosen on the position of a disk or ring with given inner and outer radii. Then the energy of the alpha particles was randomly chosen between 0-10 MeV and the resulting range in the counter gas computed. The emission angle ( $\theta$ ) and polar angle ( $\phi$ ) were randomly chosen. Using (1) from the analytical model, the position of the alpha particles was compared to the radius of the anode of the detector and area rejected when they exceeded the radius. Finally, the events were binned in energy, with 1 MeV-wide bins. An example of the results from the Monte Carlo are given by the solid "data" points in Fig. 9 where the 300 mm disk was modeled. The shaded region on Fig. 9 indicates the width of the energy bins.

Comparing the efficiency vs alpha particle energy of the Monte Carlo model to the analytical model (Fig. 9), one sees that the results from both models have similar characteristics. The efficiency is unity at the lowest alpha particle energies, then drops monotonically with energy. The differences

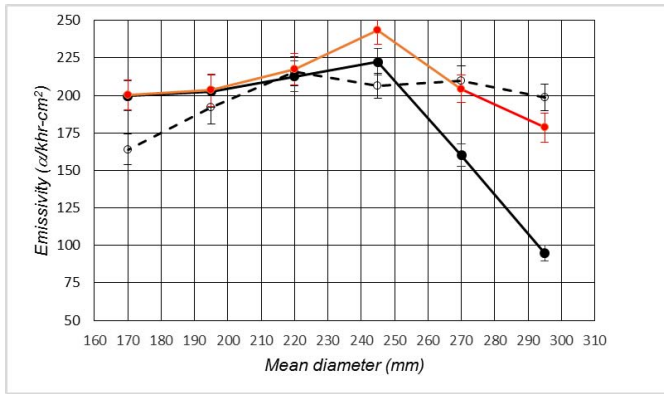


Fig. 12. The emissivity data for the Al rings with fixed outer diameter minus inner diameter of 1 cm. Solid black data points connected by a solid black line correspond to “wafer” mode, and open black data points connected by a dashed line correspond to “full” mode and the solid red data points connected by a solid red line correspond to the analytical model applied to the wafer data.

between the models is  $<10\%$  at 10 MeV, with the Monte Carlo model producing a higher efficiency.

## V. DISCUSSION OF THE RESULTS

The analytical and Monte Carlo models discussed in the last section assume *isotropic* and *homogeneous* alpha particle emission across the surface of the samples. This means that alpha particle emission from any angle, or position, on the surface of a sample is equally likely. The assumptions, however, need to be verified. A recent publication discusses alpha emitters from  $^{210}\text{Po}$  diffusing to the surface [8]. Since the detectors currently in use for the detection of ULA levels of trace contamination do not have position sensitivity, we have no way to know if the emission from the samples is homogeneous or not.

The CounterMeasure software provided with the UltraLo-1800 detector applies an efficiency correction based on an analytical model, similar to the one discussed in section IV, and assumes that the sample completely covers the active counting region (i.e., 300 mm diameter disk) [3]. That is because many samples under test are 300 mm diameter wafers, in various stages of fabrication for semiconductors.

We have applied the results of the analytical model presented in section IV to the data shown in Fig. 4 - the rings with fixed outer diameter– inner diameter of 1 cm. Instead of simply summing the number of alpha particles, we summed the reciprocal of the efficiency determined for each alpha particle determined by its energy. The emissivity data from Fig. 4, measured both in wafer mode (solid black data points connected by a solid black line), full mode (open black data points connected by a dashed black line) and the analytical model applied to the wafer data (solid red data points connected by a solid red line) is shown in Fig. 12. The corrections applied to the data ranged from 82.5% for the largest ring to 0.3% for the smallest ring. Comparison of the corrected wafer data to the data taken in wafer mode are generally within  $2\sigma$  as shown in Fig. 12. However, a larger discrepancy is observed for the samples with mean diameter

170 mm and 245 mm, which may be due to anisotropic or non-uniform emission from the rings. Further work is being undertaken to investigate the angular dependence of the alpha particle emission on the overall detection efficiency.

## VI. CONCLUSION

We have shown several examples where the alpha particle emission from rings and disks of the same material but differing in size yielded different emissivity values due to differences in detection efficiency. All alpha particles were collected with unity efficiency for small samples, but significantly lower efficiency was observed for very large samples- comparable to the size of the 300 mm diameter anode (in wafer mode). This decrease in efficiency is directly correlated to the portion of the sample under investigation that resides within the energy-dependent path length of the anode edge. For higher energy alpha particles, the effect is more pronounced and can drastically reduce the apparent emissivity depending on the sample geometry. Models based on Monte-Carlo and analytical approaches have been used to correct emissivity values based on alpha particle energy and type of sample under the assumption of isotropic emission and coaxial alignment with the detector anode. These corrections lose some accuracy in the case of anisotropic alpha particle emission.

Many of the samples measured exhibited peaks in the alpha particle energy spectra due to emission from  $^{210}\text{Po}$ . The qualitative peak shapes in the observed spectra depended on both the geometry of the sample and the measurement mode of the instrument. The peak shapes were most well defined when more of the sample area was located further from the boundary between the active counting and veto regions (i.e., small samples). However, we note that these spectra were not corrected for the energy-dependent efficiency.

## ACKNOWLEDGEMENT

The authors wish to thank their colleagues at IBM with whom they had fruitful discussions, namely K. Paul Muller, Phil Oldiges, Tak Ning, and Greg Massey.

## REFERENCES

- [1] R. Baumann, “Effects of terrestrial radiation on integrated circuits,” in *Handbook of Semiconductor Manufacturing Technology*, Y. Nishi and R. Doering, Eds., 2nd ed. Boca Raton, FL, USA: CRC Press, 2007, pp. 8–31.
- [2] R. Baumann and E. Smith, “Call for improved ultra-low background alpha-particle metrology for the semiconductor industry,” *Int. Sematech Technol. Transf., Tech. Rep. #01054118A-XFR*, 2001.
- [3] [Online]. Available: [http://xia.com/UltraLo/PDF/UltraLo-1800\\_Users\\_Manual.pdf](http://xia.com/UltraLo/PDF/UltraLo-1800_Users_Manual.pdf)
- [4] M. S. Gordon, K. P. Rodbell, H. H. K. Tang, E. Yashchin, E. W. Cascio, and B. D. McNally, “Selected topics in ultra-low emissivity alpha-particle detection,” *IEEE Trans. Nucl. Sci.*, vol. 60, no. 6, pp. 4265–4274, Dec. 2013.
- [5] M. S. Gordon *et al.*, “Ultra-low emissivity alpha-particle detection,” *IEEE Trans. Nucl. Sci.*, vol. 59, no. 6, pp. 3101–3109, Dec. 2012.
- [6] M. S. Gordon, D. F. Heidel, K. P. Rodbell, B. Dwyer-McNally, and W. K. Warburton, “An evaluation of an ultralow background alpha-particle detector,” *IEEE Trans. Nucl. Sci.*, vol. 56, no. 6, pp. 3381–3386, Dec. 2009.

- [7] M. S. Gordon *et al.*, "Alpha-particle emission energy spectra from materials used for solder bumps," *IEEE Trans. Nucl. Sci.*, vol. 57, no. 6, pp. 3252–3256, Dec. 2010.
- [8] B. M. Clark, "The distribution and transport of alpha activity in tin," *J. Microelectron. Electron. Packag.*, vol. 10, no. 2, pp. 70–73, 2013.
- [9] H. Kawasaki, B. M. Clark, T. Nishino, and M. S. Gordon, "Energy dependent efficiency in low background alpha measurements and impacts on accurate alpha characterization," *IEEE Trans. Nucl. Sci.*, vol. 62, no. 6, pp. 3034–3039, Dec. 2015.
- [10] M. S. Gordon, K. P. Rodbell, C. E. Murray, and B. D. McNally, "Measurements of radioactive contaminants in semiconductor materials," *Semicond. Sci. Technol.*, vol. 31, no. 12, p. 123003, 2016.
- [11] [Online]. Available: <http://www.srim.org/>
- [12] M. P. Ruffe, "The geometrical efficiency of a parallel-disc source and detector system," *Nucl. Instrum. Methods*, vol. 52, no. 2, pp. 354–356, 1967.
- [13] L. Ruby, "Further comments on the geometrical efficiency of a parallel-disk source and detector system," *Nucl. Instrum. Methods Phys. Res. A, Accel. Spectrom. Detect. Assoc. Equip.*, vol. 337, nos. 2–3, pp. 531–533, 1994.
- [14] N. Tsoufanidis, *Measurement and Detection of Radiation*, 2nd ed. Washington, DC, USA: Taylor & Francis, 1995, pp. 268–273.
- [15] J. T. Conway, "Geometric efficiency for a circular detector and a ring source of arbitrary orientation and position," *Nucl. Instrum. Methods Phys. Res. A, Accel. Spectrom. Detect. Assoc. Equip.*, vol. 640, no. 1, pp. 99–109, 2011.